



Comparative analysis of a new $3 \times$ PPRS parallel kinematic mechanism



Hay Azulay, Masih Mahmoodi*, Ray Zhao, James K. Mills, Beno Benhabib

Department of Mechanical and Industrial Engineering, University of Toronto, 5 King's College Road, Toronto, Ontario, Canada M5S 3G8

ARTICLE INFO

Article history:

Received 12 April 2013

Received in revised form

15 October 2013

Accepted 21 December 2013

Available online 20 January 2014

Keywords:

Parallel kinematic mechanism

Stiffness

Tilt angle

ABSTRACT

Parallel Kinematic Mechanisms (PKMs) are well suited for high-accuracy applications. However, constraints such as end-effector rotation (i.e., platform tilt angle) and configuration-dependent stiffness often limit their usage. A new six degree-of-freedom (dof) PKM architecture based on a $3 \times$ PPRS topology that addresses these concerns is presented in this paper – specifically, the proposed PKM can achieve high (end-effector) tilt angles with enhanced stiffness. The mechanism is also compared with similar three known 6-dof architectures, through which it is shown that the proposed PKM indeed exhibits higher stiffness relative to these three reference PKMs. The static stiffness is derived using matrix structural analysis, and the dynamic stiffness is obtained via finite-element analysis. A prototype of the proposed PKM that was designed and built is presented.

© 2013 Elsevier Ltd. All rights reserved.

1. Introduction

Parallel Kinematic Mechanisms (PKMs) are well suited for high-accuracy applications, such as machining, due to their superior stiffness characteristics [1]. However, some of their drawbacks, such as small workspace coverage and constrained end-effector/tool/platform rotation range of motion (tilt angle), limit them to niche applications. For example, while following a continuous path on a 3D surface, the platform of most PKMs cannot be tilted more than 90° . Furthermore, PKMs which can achieve a 90° tilt angle often do not satisfy the required stiffness for the application at hand, such as 5-axis machining.

Several different approaches have been proposed to enhance the PKMs' performance. One approach is to design hybrid mechanisms, namely, the combination of parallel and serial mechanisms. Examples include the Ecospeed [1], the Hermes, [2], the TriCenter [1], and the Metrom machine [1]. Another approach is to incorporate redundant degrees-of-freedom (dof), namely, to design PKMs with more joints than required for the task. Such redundancies can be used to enhance task allocation, via optimization, for example increasing the platform tilt angle [3–6]. The third approach is simply to design novel PKM architectures [7], such as the one proposed in this paper.

Although a large number of novel PKMs have been developed in the past [8], only a subset of these can achieve a 90° platform tilt angle – which is one of the fundamental design requirements in this work. Three well known PKMs that can achieve 90° tilt angle,

while following a path on a 3D surface, all comprise three chains with prismatic joint that moves on a circular guide: the Alizade mechanism, with a $3 \times$ PPRS topology [9], the Eclipse, with a $3 \times$ PPRS topology [10], and the Glzman mechanism, with a $3 \times$ PPRS topology [7]. Hereafter, these PKMs are referred to as the reference PKMs.

Three other PKMs, similar to the above 6-dof reference PKMs include: the Behi PKM [11], which is based on a $3 \times$ PPRS topology similar to that of the Alizade mechanism, the Tahmasebi PKM that has a $3 \times$ PPRS topology [12], and the Ben-Horin PKM that has a $3 \times$ PPRS topology [13]. The Behi PKM can be configured with a triangular or a rectangular base, and the Tahmasebi, and Ben-Horin PKMs' base joints can be fixed at different locations prior to operation. However, since each of the joints in these PKMs can only move along linear paths, their workspace coverage would be tangibly smaller than the reference PKMs, when designed with similar dimensions [14].

One may note that, some PKMs with 5-dof or less can also achieve 90° tilt angle; however, their motions are often coupled. Furthermore, such low-mobility spatial mechanisms require either extra passive chains (e.g., [15,16]), or specific geometrical relations between the joints (e.g., [17]), which may result in geometrical interference, leading to limited workspace coverage [18].

The objective of this paper is, thus, to present a new $3 \times$ PPRS PKM architecture developed and built in our laboratory. The proposed PKM exhibits a 90° tilt angle and its static stiffness and dynamic stiffness are tangibly better than those of the three reference PKM architectures, namely, the Eclipse, the Alizade PKM, and the Glzman PKM. The primary application for our proposed novel mechanism is its use as a high-accuracy meso-Milling Machine Tool (mMT) [19]. Design of such machines with the required stiffness is a challenge due to their scaled-down structures.

* Corresponding author.

E-mail addresses: h.azulay@utoronto.ca (H. Azulay), masih.mahmoodi@utoronto.ca (M. Mahmoodi), rayzhao@mie.utoronto.ca (R. Zhao), mills@mie.utoronto.ca (J.K. Mills), benhabib@mie.utoronto.ca (B. Benhabib).

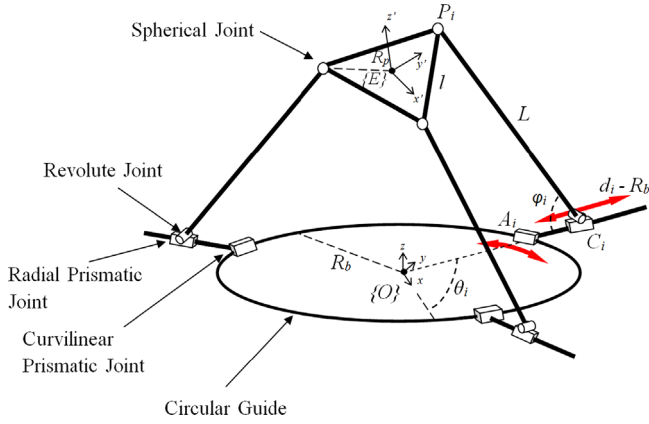


Fig. 1. Kinematic notation for the proposed PKM.

2. Proposed parallel kinematic mechanism

The proposed $3 \times$ PPRS PKM is shown in Fig. 1. The mechanism consists of three kinematic chains, each chain consists of a circular guide of radius, R_b , on which two prismatic joints (pairs) are mounted. The first prismatic joint, which moves on a circular guide, is, herein, referred to as the *curvilinear* prismatic joint. The second prismatic joint, which moves in radial direction with respect to the circular guide, is, herein, referred to as *radial* prismatic joint. It is mounted on the curvilinear prismatic joint. The global coordinate system, $\{O\}$, is positioned at the center of the circular guide. The position of the curvilinear prismatic joint of the i th chain is denoted as $A_i = [A_{ix} \ A_{iy} \ A_{iz}]^T$, ($i=1-3$). The position of the radial prismatic joint is denoted as $C_i = [C_{ix} \ C_{iy} \ C_{iz}]^T$.

Three links of fixed length L connect the radial prismatic joints to the mobile platform through passive revolute and spherical joints, respectively. The angular travel of the revolute joints are denoted as φ_i , and each revolute joint is rotating about an axis that is tangential to the circular guide. The Cartesian positions of the spherical joints are denoted as $P_i = [P_{ix} \ P_{iy} \ P_{iz}]^T$.

The joint-space generalized coordinates of the active joints are defined by the vector $Q = [\theta_1 \ \theta_2 \ \theta_3 \ d_1 \ d_2 \ d_3]^T$, where θ_i represents the curvilinear prismatic joint travel, and d_i represents the radial prismatic joint travel, respectively. A moving Frame, $\{E\}$, is attached to the center of the platform, where its z -axis is normal to the platform plane. The vector $X_{pc} = [x_{pc} \ y_{pc} \ z_{pc} \ \alpha \ \beta \ \gamma]^T$ represents the position and orientation (pose) of Frame $\{E\}$, with respect to the Global Frame $\{O\}$. α , β , and γ are the Euler angles for the ZYZ transformation-order matrix. The angles α and β are selected according to the orientation of the platform normal, which is required for the task. Since γ is redundant for 5-axis machining, it can be optimized so that the PKM configuration with the highest stiffness is chosen.

2.1. Kinematics

The positions of the spherical joints, P_i ($i=1-3$), in task-space coordinates can be obtained from the pose of the platform Frame, $\{E\}$, as

$$P_i = [x_{pc} \ y_{pc} \ z_{pc}]^T + R^E P_i, \quad (1)$$

where P_i is the position of the i th spherical joint given in task-space coordinates, R is the rotation matrix of the platform with respect to the Global Frame, and ${}^E P_i$ is the position of the i th spherical joint with respect to the platform Frame, $\{E\}$.

The joint-space coordinates of the PKM, in terms of the position of the spherical joints, are expressed as

$$\theta_i = \tan^{-1}(P_{iy}/P_{ix}), \quad (2)$$

$$\varphi_i = \sin^{-1}(P_{iz}/L), \quad \text{and} \quad (3)$$

$$d_i = \sqrt{L^2 - P_{iz}^2} + \sqrt{(P_{ix}^2 + P_{iy}^2)}. \quad (4)$$

Given Eqs. (1)–(4), the positions of the curvilinear and radial prismatic joints can be obtained as

$$A_i = [R_b \cos \theta_i \ R_b \sin \theta_i \ 0]^T, \quad (5a)$$

$$C_i = [d_i \cos \theta_i \ d_i \sin \theta_i \ 0]^T. \quad (5b)$$

In direct kinematics, the platform pose is obtained from the set of active joint variables, d_i and θ_i . The platform pose is determined as follows: (i) the spherical joints' positions are determined from the set of active joint variables, and consequently (ii) the platform pose is obtained from the passive spherical joints' positions. Considering the geometrical constraint on the link length, L , the location of the spherical joints can be expressed as

$$P_i = \begin{bmatrix} (d_i - L \cos \varphi_i) \cos \theta_i \\ (d_i - L \cos \varphi_i) \sin \theta_i \\ L \sin \varphi_i \end{bmatrix}. \quad (6)$$

The passive joints variables, φ_i , which are required in order to obtain P_i , can be determined from the geometrical constraints on the platform shape. Assuming the platform is an equilateral triangle, the geometrical constraint on the platform side length, l , can be expressed as

$$\|P_i - P_j\| = l^2; \quad i, j = 1, 2, 3; \quad i \neq j. \quad (7)$$

Combining Eqs. (6) and (7), the following set of three equations is derived:

$$\begin{aligned} & [(d_i - L \cos \varphi_i) \cos \theta_i - (d_j - L \cos \varphi_j) \cos \theta_j]^2 + \\ & [(d_i - L \cos \varphi_i) \sin \theta_i - (d_j - L \cos \varphi_j) \sin \theta_j]^2 + \\ & [L \sin \varphi_i - L \sin \varphi_j]^2 = l^2; \quad i, j = 1, 2, 3; \quad i \neq j. \end{aligned} \quad (8)$$

where the unknown variables are φ_i .

The set of equations, represented by (8), can be converted into a system of polynomial equations in term of t_i , by substituting the following trigonometric identities:

$$t_i = \tan\left(\frac{\varphi_i}{2}\right); \quad \cos \varphi_i = \frac{1 - t_i^2}{1 + t_i^2}; \quad \sin \varphi_i = \frac{2t_i}{1 + t_i^2}. \quad (9)$$

The resulting non-linear system has four unique solutions for t_1 , t_2 , and t_3 . A more detailed solution of the above equations can be found in Ref. [13]. Finally, once the spherical joints' positions are obtained, the platform center point position, CP , is derived:

$$CP = \frac{\sum_{i=1}^3 P_i}{3}, \quad (10)$$

as well as the platform orientation, OR :

$$OR_x = \frac{P_1 - PC}{l/\sqrt{3}}, \quad (11)$$

$$OR_y = \frac{P_2 - P_3}{l}, \quad (12)$$

$$OR_z = OR_x \times OR_y. \quad (13)$$

2.2. Dynamics

The dynamic equations of motion of the proposed PKM can be obtained using Lagrange’s formulation and the principle of energy equivalence. The principle of energy equivalence states that the dynamic behavior of a generic PKM is equivalent to the combined dynamics of all serial chains and the dynamics of the moving platform [20–22]. The approach given here for the derivation of dynamic equations extends our preliminary work reported in Ref. [20], which involves disassembling the PKM at the platform’s spherical joints. The resulting system consists of three serial chains and a moving platform. Since no external forces are applied on the passive joints, our objective is to derive the equations of motion of the proposed PKM in terms of the active joint coordinates, Q , only.

Let us define $q_i = [\theta_i \ d_i \ \varphi_i]^T$ as the vector of joint-space coordinates for the i th kinematic chain ($i=1-3$). Utilizing Lagrange’s method, the dynamics of each serial chain is obtained as

$$\mathbf{M}_{qi}\ddot{q}_i + C_{qi} + g_{qi} = \tau_{qi}, \quad (14)$$

where \mathbf{M}_{qi} is the inertia matrix, C_{qi} , and g_{qi} are the vectors of centrifugal/Coriolis terms, and the gravity vector, respectively. τ_{qi} is the vector of generalized forces at the joints. Evaluating the time derivative of the spherical joint coordinates given in Eq. (6) yields

$$\dot{p}_i = \mathbf{W}_i \dot{q}_i, \quad (15)$$

where \mathbf{W}_i is a 3×3 matrix, which transforms the joint-space velocities of the i th serial chain, \dot{q}_i , to the velocity of the associated spherical joint, \dot{p}_i . The spherical joint velocity, on the other hand, can be obtained, given the platform geometry, its angular velocities, and its center point linear velocities, which are denoted as $V_{pc} = [\dot{x}_{pc} \ \dot{y}_{pc} \ \dot{z}_{pc} \ \Omega_x \ \Omega_y \ \Omega_z]^T$. The velocity of the platform i th spherical joint can be expressed as

$$\dot{p}_i = \mathbf{U}_i V_{pc}, \quad (16)$$

where \mathbf{U}_i is a 3×6 matrix, which transforms V_{pc} , to \dot{p}_i . Utilizing the kinematic expressions (15) and (16), and the principle of energy equivalence, the dynamics of the entire PKM is expressed as

$$(\mathbf{M}_p \dot{V}_{pc} + C_p + g_p) + \sum_{i=1}^3 (\mathbf{M}_i \dot{V}_{pc} + C_i + g_i) = \tau_{pc}. \quad (17)$$

where \mathbf{M}_p is the inertia matrix of the platform, C_p , and g_p are the vectors of centrifugal/Coriolis terms, and the gravity vector of the platform, respectively. \mathbf{M}_i is the inertia matrix of the i th serial chain. Similarly, C_i and g_i are the centrifugal/Coriolis terms, and the gravity vector. Detailed matrix expressions for \mathbf{M}_i , C_i , and g_i are as follows:

$$\mathbf{M}_i = (\mathbf{Z}_i)^T \mathbf{M}_{qi} \mathbf{Z}_i, \quad (18)$$

$$C_i = (\mathbf{Z}_i)^T \mathbf{M}_{qi} (\mathbf{W})^{-1} \left[\frac{d}{dt} (\mathbf{U}_i) \right] (\mathbf{Z}_i)^{-1} \dot{q}_i + (\mathbf{Z}_i)^T \left(\mathbf{M}_{qi} \left[\frac{d}{dt} (\mathbf{W})^{-1} \right] (\mathbf{Z}_i)^{-1} \dot{q}_i + C_{qi} \right), \quad \text{and} \quad (19)$$

$$g_i = (\mathbf{Z}_i)^T g_{qi}, \quad (20)$$

where \mathbf{Z}_i is the transformation between the generalized velocities of the i th serial chain to the platform angular and center point linear velocities as

$$\dot{q}_i = \mathbf{Z}_i V_{pc} = \mathbf{W}_i^{-1} \mathbf{U}_i V_{pc}. \quad (21)$$

In Eq. (17), τ_{pc} is the vector of generalized forces acting on the PKM, which contains the vector of external forces, denoted by τ_{ext} , and the vector of the transformed generalized forces, denoted by

τ_{qi} , as follows:

$$\tau_{pc} = \tau_{ext} + \sum_{i=1}^3 (\mathbf{Z}_i)^T \tau_{qi}, \quad (22)$$

where τ_{ext} acts on the platform, and τ_{qi} acts on the PKM joints. All the dynamic matrices and vectors in Eq. (17) are represented with respect to task-space coordinates.

The obtained task-space dynamic model of the PKM, as given in Eq. (17) is transformed to active joint-space coordinates. To this end, the geometric Jacobian of the PKM, \mathbf{J}_G , which relates the active joint-space velocities to the platform center point linear velocities and platform angular velocities, is obtained as follows:

$$\mathbf{J}_G \dot{Q} = V_{pc}. \quad (23)$$

The geometric Jacobian is obtained in a two-step process. In the first step, the analytical Jacobian, \mathbf{J} , is derived by evaluating the time derivative of the kinematic relations between the task-space variables, X_{pc} , and the active joint-space variables Q :

$$\dot{Q} = \mathbf{J}^{-1} \dot{X}_{pc}. \quad (24)$$

In the second step, the geometrical Jacobian, \mathbf{J}_G , is obtained by

$$\mathbf{J}_G = \mathbf{H} \mathbf{J}, \quad (25)$$

where \mathbf{H} is the ZYZ Euler angles transformation matrix that relates the angular rate of change corresponding to the analytical Jacobian to the angular velocities of the task-space variables corresponding to the geometric Jacobian [23]. Detailed expression for \mathbf{H} is given by

$$\mathbf{H} = \begin{pmatrix} 1 & 0 & 0 & 0 & 0 & 0 \\ 0 & 1 & 0 & 0 & 0 & 0 \\ 0 & 0 & 1 & 0 & 0 & 0 \\ 0 & 0 & 0 & 0 & -\sin \alpha & \cos \alpha \sin \beta \\ 0 & 0 & 0 & 0 & \cos \alpha & \sin \alpha \sin \beta \\ 0 & 0 & 0 & 1 & 0 & \cos \beta \end{pmatrix}. \quad (26)$$

Using the geometric Jacobian matrix, the transformed dynamic equations of the proposed PKM to active joint-space coordinates are expressed as

$$\mathbf{M}_Q \ddot{Q} + C_Q + g_Q = \tau_Q, \quad (27)$$

where \mathbf{M}_Q is the inertia matrix of the PKM, C_Q , and g_Q are the vectors of centrifugal/Coriolis terms, and the gravity vector of the PKM, respectively. The matrix expressions of the final dynamic equations of motion in terms of active joint-space coordinates are

$$\mathbf{M}_Q = \mathbf{J}_G^T \mathbf{M}_t \mathbf{J}_G, \quad (28)$$

$$C_Q = (\mathbf{J}_G)^T \mathbf{M}_t \frac{d}{dt} (\mathbf{J}_G) V_{pc} + (\mathbf{J}_G)^T C_t, \quad \text{and} \quad (29)$$

$$g_Q = (\mathbf{J}_G)^T g_t, \quad (30)$$

where

$$\mathbf{M}_t = \mathbf{M}_p + \sum_{i=1}^3 \mathbf{M}_i, \quad C_t = C_p + \sum_{i=1}^3 C_i, \quad g_t = g_p + \sum_{i=1}^3 g_i. \quad (31)$$

τ_Q is the active-joint space vector of generalized forces applied on the joints of the PKM, as follows:

$$\tau_Q = (\mathbf{J}_G)^T \tau_{pc}. \quad (32)$$

3. PKM kinematic and stiffness analysis

In this section, the proposed PKM is analyzed in terms of its platform tilt angle, singularities, and stiffness.

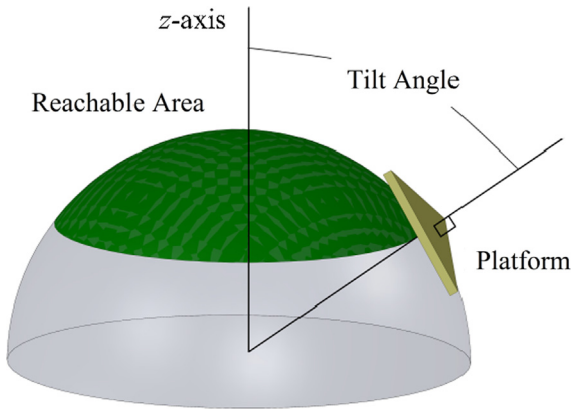


Fig. 2. Hemispherical workspace/workpiece.

Table 1
Dimensions of the proposed PKM.

Design parameter	Proposed PKM
Base radius (R_b)	162 mm
Platform radius (R_p)	18 mm
Link Length (L)	216 mm
Curvilinear prismatic joint's range of travel (θ_i)	Continuous 360°
Radial prismatic joint's range of travel ($d_i - R_b$)	0–65 mm
Revolute joint's range of travel (φ_i)	5–70°
Spherical joint's range of travel	$\pm 70^\circ$

3.1. Platform tilt angle

A PKM's tilt angle is typically defined as the maximal reachable angle of the platform over a spherical surface, while being tangent to its surface. The angle is measured from the z-axis, as shown in Fig. 2. The spherical surface is discretized herein into a finite number of points, and the platform center point ability to reach them is evaluated through kinematic simulation of the proposed PKM, while taking into account geometrical interferences. The dimensions/constraints of the PKM, which are incorporated into the kinematic simulations, are presented in Table 1.

In our study, the link length of the proposed PKM was varied to determine the dimension, for which the platform could reach at least 90° tilt angle. Some analysis examples of platform tilt angle versus the radius of the workpiece sphere are shown in Fig. 3. It should be noted that although the link length of 196 mm would lead to a better tilt angle achievement for the proposed PKM, a 216 mm link was employed in this paper in order to achieve a fair comparison with other mechanisms, as will be further discussed in Section 4.

3.2. Singularities

The kinematic singularities of PKMs are typically defined with respect to the Jacobian matrix, \mathbf{J} , and classified into three types [18]. Evaluating the time derivative of the kinematic relations of the PKM, one can obtain:

$$\mathbf{J}_q \dot{\mathbf{Q}} = \mathbf{J}_x \dot{\mathbf{X}}_{pc}, \quad (33)$$

where \mathbf{J}_q and \mathbf{J}_x are the matrix of the time derivatives of the joint-space variables, and the matrix of the time derivatives of the task-space variables, respectively. The Jacobian can be expressed as

$$\mathbf{J} = \mathbf{J}_x^{-1} \mathbf{J}_q. \quad (34)$$

For the proposed PKM, the closed-form solution for \mathbf{J}^{-1} can be derived. Hence, the PKM singularities are classified according to

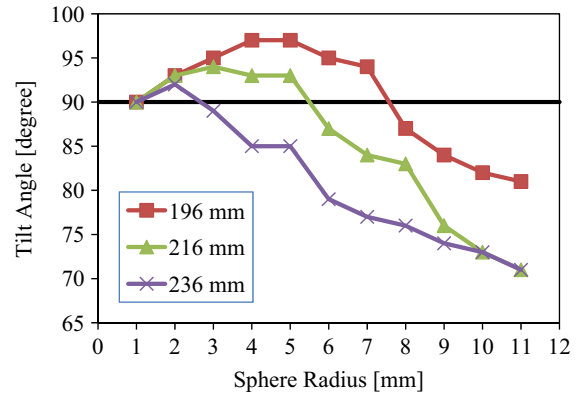


Fig. 3. The platform tilt angle of the proposed PKM for different link lengths.

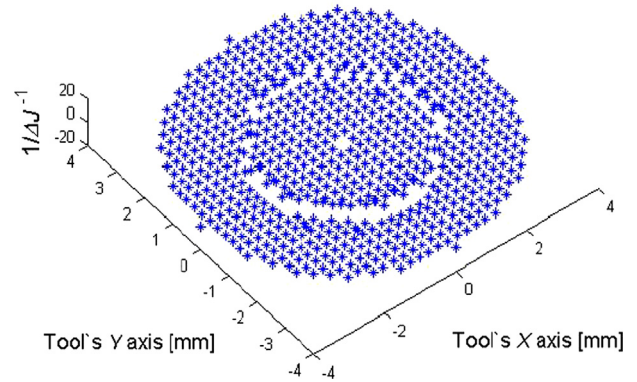


Fig. 4. Distribution of $1/\Delta\mathbf{J}^{-1}$ over the hemisphere.

the Jacobian determinant, $\Delta\mathbf{J}^{-1}$, as follows:

$$\begin{cases} \Delta\mathbf{J}^{-1} = \pm \infty & \Delta\mathbf{J}_q = 0 & \text{Type 1 singularity} \\ \Delta\mathbf{J}^{-1} = 0 & \Delta\mathbf{J}_x = 0 & \text{Type 2 singularity} \end{cases} \quad (35)$$

Type 1 singularity (or, serial singularity) results in a non-zero velocity vector, $\dot{\mathbf{Q}}$, for which the platform does not move. Type 2 singularity (or parallel singularity) leads to a non-zero motion, $\dot{\mathbf{X}}_{pc}$, for which the joint velocities, $\dot{\mathbf{Q}}$, are zero. Type 3 singularity occurs when both Type 1 and Type 2 singularities are present at the same time.

Note that since the Jacobian matrix is not homogeneous in terms of units, its determinant value may not have a physical meaning when it is at a singular configuration ($\Delta\mathbf{J}^{-1} = 0$ or $\infty \pm$). The Jacobian matrix terms are non-homogenous when (i) a combination of joints (i.e., revolute and prismatic) are used and (ii) the PKM has translational and rotational dof [24]. Therefore, the “closeness” of a 6-dof PKM configuration to singularity can be only realized with respect to the distribution of Jacobian determinant over the workspace. For example, a configuration is considered to be singular when the Jacobian determinant is high compared to determinants of other configurations.

Simulations that analyze PKM configurations at discretized points over the workspace can identify singularities. This can be achieved through calculation of the Jacobian determinant, or through evaluation of the Condition Number (CN) [18,23].

Fig. 4 shows values of $1/\Delta\mathbf{J}^{-1}$ of the proposed PKM at discrete task-space locations on the surface of a 4 mm radius hemispherical workpiece. As can be noted, the graph contains a circular area at about $r=2$ mm, which is the result of higher/lower $1/\Delta\mathbf{J}^{-1}$ values. This indicates that the associated configurations are close to singularity. The singularities shown in Fig. 4 are of Type 2 singularity.

3.3. Stiffness

The accuracy of a PKM is directly related to its static and dynamic stiffness. Static stiffness indicates the resistance of the structure to deflection when the loading conditions are not time dependent. Dynamic stiffness, on the other hand, indicates the magnitude of the vibration response of the mechanism in the presence of time-varying loading. Both the static stiffness and the dynamic stiffness are highly related to the PKM architecture, and to the specific PKM configuration [1]. Thus, it is important to identify PKM architectures that combine on the one hand the ability to achieve 90° tilt angle, while following a path on a 3D surface, and on the other hand maintaining high stiffness at the platform center point.

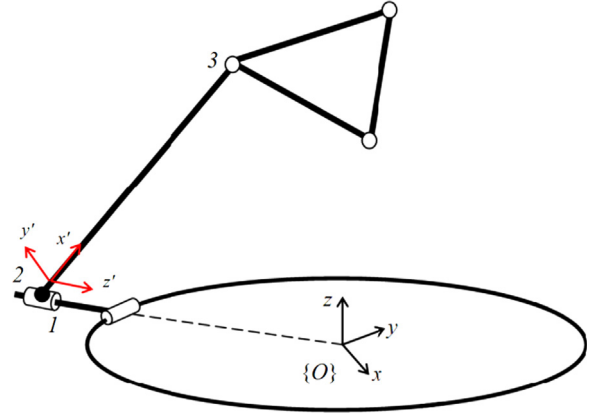


Fig. 5. Coordinate notation for the proposed PKM static stiffness model.

3.3.1. Static stiffness

Several methods have been proposed for the analytical modeling of static stiffness of PKMs [25–28]. These methods consider the contribution of each chain separately, and by combining the joints' boundary conditions, the overall stiffness matrix of the PKM is constructed. The motivation in developing these methods has been to provide a quick evaluation of static stiffness in relation to the PKM configuration. It should be noted that, in our simulations, the platform is required to be tangent to the hemispherical surface at every discretized point on its surface, as shown in Fig. 2. Therefore, the tool orientation can be defined by two Euler angles. Since the third angle, which is the roll angle about the tool axis, is redundant for the task, an optimization can be performed to determine the angle that leads to the configuration with the highest stiffness [29].

The static stiffness of the PKM at the center point of the platform is obtained herein using the Matrix Structural Analysis (MSA) method [30]. The reason for choosing the MSA approach is that, unlike Finite Element Analysis (FEA), MSA can quickly evaluate the stiffness distribution within the workspace. The structural components that are considered in the modeling of the PKMs are the joints and the links. The following gives an overview on the procedure for evaluating the static stiffness:

1. The PKM's links are modeled as beam elements, with each element consisting of two nodes. The elements allow for bending deformations in the two lateral directions with respect to the beam orientation as well as axial deformation along the beam. The stiffness matrix, K^i , of the i th element is represented with respect to its local frame. The matrix is assembled from four sub-matrices as shown in Eq. (36):

$$K^i = \begin{bmatrix} K_{11}^i & K_{12}^i \\ K_{21}^i & K_{22}^i \end{bmatrix}, \quad (36)$$

where K_{jk}^i ($j,k=1,2$) are the stiffness matrices of the first and second nodes of element i .

2. The link stiffness matrix is transformed from the link local frame to the Global Frame, $\{O\}$, using the rotation matrices between the frames, Fig. 5.
3. The transformed stiffness matrix of each mechanism chain, K_T , is assembled according to the boundary conditions on each link as shown in Fig. 6.

$$K_T = \begin{bmatrix} K_{11}^1 & K_{12}^1 & 0 \\ K_{21}^1 & K_{22}^1 + K_{11}^2 & K_{12}^2 \\ 0 & K_{21}^2 & K_{22}^2 \end{bmatrix};$$

$$K_T = \begin{bmatrix} K_{11}^1 & K_{12}^1 & 0 & 0 \\ K_{21}^1 & K_{22}^1 & 0 & 0 \\ 0 & 0 & K_{11}^2 & K_{12}^2 \\ 0 & 0 & K_{21}^2 & K_{22}^2 \end{bmatrix}; \quad K_T = \begin{bmatrix} K_{11}^1 & 0 & 0 \\ 0 & K_{11}^2 & K_{12}^2 \\ 0 & K_{21}^2 & K_{22}^2 \end{bmatrix}$$

4. Linkage constraints between links are considered through matrices that describe the kinematic relations between the nodes on the two sides of the joint. These constraints are assembled into a matrix, A_k , according to the nodes numbers.
5. Evaluating the extremum of the total potential energy under the kinematic constraints using Lagrange multipliers, leads to the following set of equations:

$$\begin{bmatrix} K_T & A_K^T \\ A_K & 0 \end{bmatrix} \begin{bmatrix} \Delta X \\ \lambda_M \end{bmatrix} = \begin{bmatrix} F \\ 0 \end{bmatrix}, \quad (37)$$

where, λ_M is the Lagrange multipliers vector, F is the force vector applied on the nodes, and ΔX is the vector of the displacements of the nodes dof. The displacements of all the chain's nodes can be determined from Eq. (37).

6. The stiffness matrix of the mechanisms is constructed in a similar way to Step (4), using the three chains stiffness matrices obtained in Step (5). All four PKMs compared in this paper are modeled according to the model shown in Fig. 7 where the links are represented by Nodes 1–3. The platform elements are modeled as rigid connections, and the associated Nodes are 4–7. Subsequently, the static stiffness of the mechanism is evaluated at Node 7, which is the platform center point.

Static stiffness has been shown to be related to the Jacobian matrix [31], hence, simplified stiffness indices based on the CN have been proposed [32]. However, the applicability of these indices is limited to Jacobian matrices that are homogeneous in terms of units. Hence, the stiffness of a 6-dof PKM cannot be evaluated only based on its Jacobian matrix. In order to overcome these challenges, a statistical framework for the analysis of the stiffness is presented here:

1. Determine the stiffness along x , y , and z axes at a large number of discretized check points (317 in our simulations), preferably over a hemispherical surface, while the platform is tangent to the surface. Since the PKM has 6-dof, at each check point there are infinite possible PKM configurations depending on the platform roll angle, i.e., the rotation about the axis normal to the platform. Moreover, referring to side-milling of a groove,

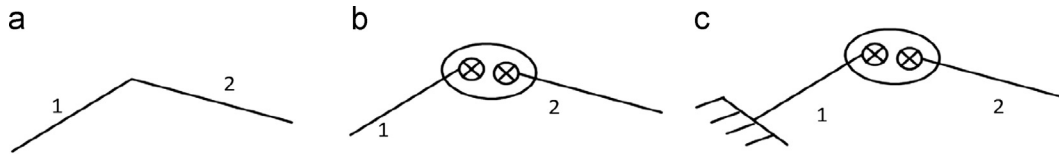


Fig. 6. Stiffness matrix assembly: (a) two beams with rigid connection, (b) two beams connected by a revolute joint, and (c) two beams connected by a revolute joint when the first beam is fixed to the base.

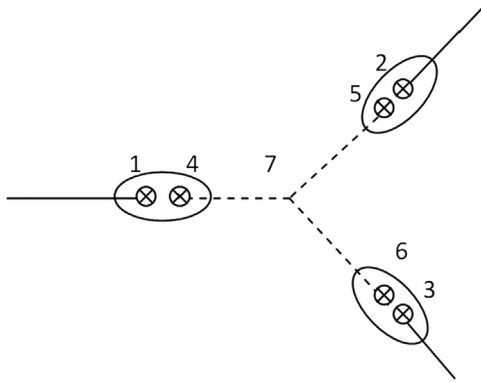


Fig. 7. Schematics of the overall proposed PKM.

Table 2
Mean and variance values of PKMs' static stiffness distribution.

Stiffness	Statistical analysis	Link length [mm]		
		196	216	236
K_{xx} [N/ μm]	Mean	5.74	5.69	5.28
	Variance	0.24	0.38	0.39
K_{yy} [N/ μm]	Mean	5.49	4.73	4.21
	Variance	0.22	0.33	0.33
K_{zz} [N/ μm]	Mean	8.77	5.43	3.92
	Variance	1.18	0.21	0.10

the milling force acting on the tool tooth has three components: F_t , the force in the direction of the cutting, F_r , the force in radial direction to the tool, and F_a , the axial force. The cutting forces oscillate with respect to the cutter location. However, for the given trajectories, the part can be oriented with respect to the Cartesian axis so that the maximal forces along the trajectory (on the yz plane) will be applied normal to the feed direction F_N , along the x -axis. Thus, the redundant dof is used for maximizing the stiffness along the x -axis. It should be noted that the static stiffness of the mechanism is not evaluated within the neighborhood of singularities. Such incidents are filtered based on the CN values.

- Determine the arithmetic mean and standard deviation of the stiffness values calculated in Step (1).

The links for all PKMs were modeled as tubes with outer diameter of 19 mm, and inner diameter of 14 mm. The material selected for the structure of the PKMs was steel, AISI 1018. The static stiffness of the joints was taken to be 3 N/ μm , [33] for the stiffness of ultrasonic piezo actuators. In the following simulations, the location of the workpiece with respect to the base is the same for all link lengths.

The mean and variance values of the stiffness components, K_{xx} , K_{yy} , and, K_{zz} , as a function of the link lengths are shown in Table 2.

3.3.2. Dynamic stiffness

The dynamic stiffness analysis is conducted on the proposed PKM to predict the displacement of the center point of the

platform when the PKM is subjected to dynamic loading. Herein, the dynamic stiffness of PKMs at a given configuration is defined as the ratio of the amplitude of the applied oscillating forces, to the amplitude of the vibration at the center point of the platform. Unlike the static stiffness, which is only related to the stiffness matrix of the PKM, the dynamic stiffness of the PKM also depends on the mass of its structural components, and the equivalent damping constant.

The dynamic stiffness matrix of a PKM structure, \mathbf{K}_D , at the center point of the platform can be expressed as follows [33]:

$$\mathbf{K}_D = \sqrt{(\mathbf{K} - \mathbf{M}\omega^2)^2 + (\mathbf{B}\omega)^2}, \quad (38)$$

where \mathbf{M} , \mathbf{B} , and \mathbf{K} are the structural mass matrix, equivalent damping constant matrix, and static stiffness of the PKM, respectively. ω is the frequency of the external force applied at the center point of the platform. When the frequency of the applied forces is equal to one of the natural frequencies of the PKM, the dynamic stiffness reaches its minimum, causing the displacement at the platform center point to reach its maximum [34]. Thus, it is necessary to obtain the minimum dynamic stiffness magnitudes, which can be used as an index for the accuracy of the PKM during operation.

The dynamic stiffness of a PKM at a given frequency can be obtained by inverting the Frequency Response Function (FRF). In this paper, the dynamic stiffness, which takes into account the contribution of the PKM linkages, is calculated by examining FRFs results obtained from FEA.

The Cartesian FRFs of the PKM are calculated using a commercial FEA software package, ANSYS. Harmonic analysis is conducted on the PKM being at its home configuration with the chains located in tri-axi-symmetric positions. The home configuration is the PKM posture that allows its platform center point to touch the north pole of the hemisphere while the platform is tangent to its surface. The joints' bearings are modeled using sliding contact between the pin and the housing. The equivalent damping ratio for the PKM structure is assumed to be 1%. This damping ratio accounts for the interfacial slip damping in the contacting surfaces such as revolute and sliding joints, as well as the material damping of the PKM.

3.3.3. Simulations

Simulations were conducted as three sets. In the first set, a sinusoidal force of 1 N magnitude was applied to the platform center point along the x -axis. The harmonic force represents loads created during milling operations [34]. The Cartesian displacement of the platform center point is captured along the x -axis. The Cartesian xx component of the FRFs of the proposed PKM as a function of the link lengths are shown in Fig. 8(a). In the second simulation set, the force and displacement are being applied and captured along the y -axis (Fig. 8(b)). In the third set, the force and displacement are being applied and captured along the z -axis (Fig. 8(c)).

The results show a general trend of increasing the peak amplitude of the FRFs when the link length increases. This implies that the minimum dynamic stiffness decreases as the link length increases.

4. Comparative analysis

In this paper, we compare the stiffness of four 6-dof PKMs that are based on a three-chain topology. Fig. 9(a)–(d) illustrates the schematics of these PKMs, where the last figure is our new proposed PKM.

All the PKMs' architectures are modeled using similar geometrical parameters and constraints – each chain contains two active joints. The first prismatic joint, M_1 , moves along a circular guide, which is mounted on the base. The second joint, M_2 , is mounted on M_1 . In addition, each chain includes a revolute joint and a spherical joint, which are passive. The latter is connected to the

moving platform. The primary difference between the proposed PKM and the reference PKMs lies in the positioning of M_2 .

The dimensions of the PKMs were chosen as close as possible to each other while achieving at least 90° tilt angle, as shown in Table 3. In specific cases, when it was not possible to have both criteria applied simultaneously, the condition for 90° tilt angle was preferred. For example, the Glozman PKM workspace coverage is sensitive to link-length change – where only with a link length of $(2 \times) 130$ mm, which is the closest to the dimension of the other PKMs links, that the PKM could reach the 90° tilt angle. Also, the link length of the Alizade PKM is defined at the middle of the prismatic joint travel range.

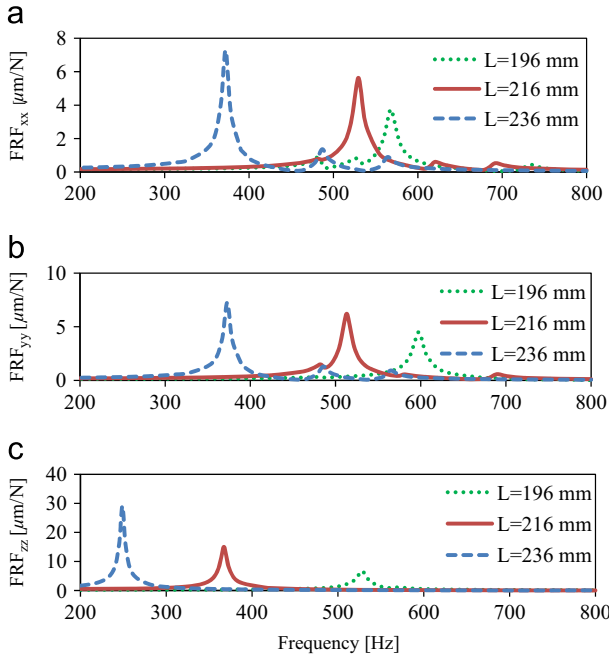


Fig. 8. Cartesian FRFs of the proposed PKM as a function of link length: (a) FRF_{xx} , (b) FRF_{yy} , and (c) FRF_{zz} .

4.1. Static stiffness

The procedure used in Section 3.3.1 for calculating the representative static stiffness of the proposed PKM is utilized here for comparing the four PKMs' architectures. Table 4 summarizes the means and variances of the static stiffness of the PKMs. Fundamental two-tailed, null-hypothesis analysis clearly shows that the proposed PKM has better stiffness properties than those of the reference PKMs, beyond a significance level of 99%.

The mean stiffness of the proposed PKM is higher than the mean stiffness of the Alizade PKM in all directions. This is due to the prismatic joints' stiffness along their direction of motion. In the case of the Alizade PKM, the joints reduce the stiffness along the links' axes, which mainly affects its stiffness along the z-axis. The proposed PKM is stiffer than the Eclipse mechanism along the x and y axes. The Eclipse vertical prismatic link in each chain acts as a cantilever beam reducing the stiffness along the x and y axes. Along the z axis, the Eclipse is stiffer than the proposed PKM, where the lower stiffness of the proposed PKM is related to its first link, which acts as a cantilever beam about the z axis. The mean stiffness of the proposed PKM is also higher than that of the Glozman PKM. In the Glozman PKM, the first link acts as a cantilever beam, which affects the stiffness along all axes, depending on the orientation of these links.

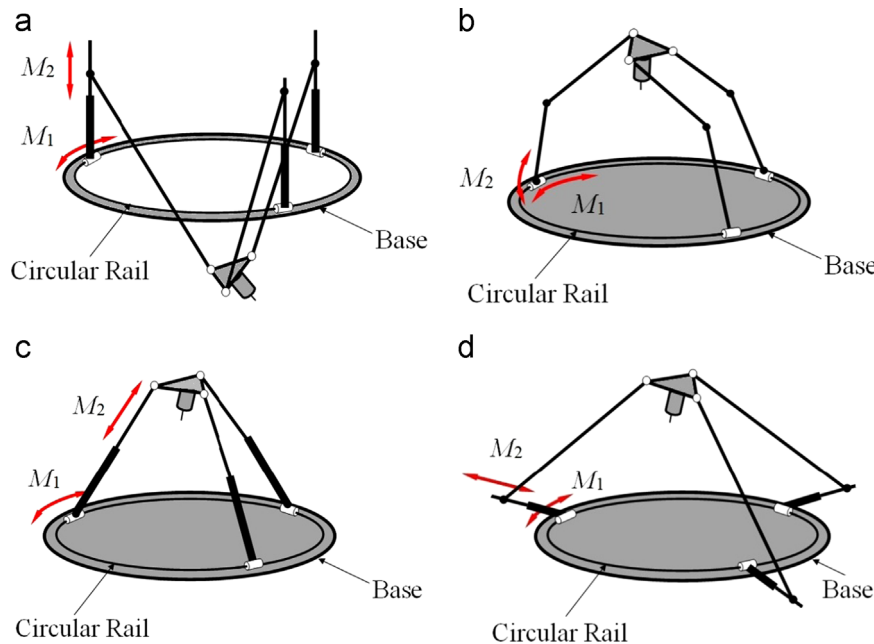


Fig. 9. Compared PKMs: (a) Eclipse, (b) Glozman PKM, (c) Alizade PKM, and (d) Proposed PKM.

Table 3
Dimensions of the PKMs.

Design parameter	Proposed PKM	Eclipse PKM	Alizade PKM	Glozman PKM
Base radius (R_b)	162 mm	162 mm	162 mm	162 mm
Platform radius (R_p)	18 mm	18 mm	18 mm	18 mm
Link length ($\ P_i - C_i\ $)	216 mm	216 mm	216 mm	130 mm
Curvilinear prismatic joint's range of travel (θ_i)	Continuous 360°	Continuous 360°	Continuous 360°	Continuous 360°
Radial prismatic joint's range of travel ($d_i - R_b$)	65 mm	65 mm	65 mm	–
Revolute joint's range of travel (φ_i)	5–70°	5–70°	5–70°	5–70°
Spherical joint's range of travel	$\pm 70^\circ$	$\pm 70^\circ$	$\pm 70^\circ$	$\pm 70^\circ$
Platform tilt angle	94°	98°	96°	96°

Table 4
Mean and variance values of PKMs' static stiffness distribution.

Stiffness	Statistical analysis	Proposed PKM	Eclipse PKM	Alizade PKM	Glozman PKM
K_{xx} [N/ μm]	Mean	5.691	4.450	3.686	2.433
	Variance	0.349	0.237	0.028	0.020
K_{yy} [N/ μm]	Mean	4.710	3.986	3.247	2.038
	Variance	0.316	0.100	0.103	0.053
K_{zz} [N/ μm]	Mean	5.690	7.360	3.601	5.487
	Variance	0.228	0.004	0.108	0.292

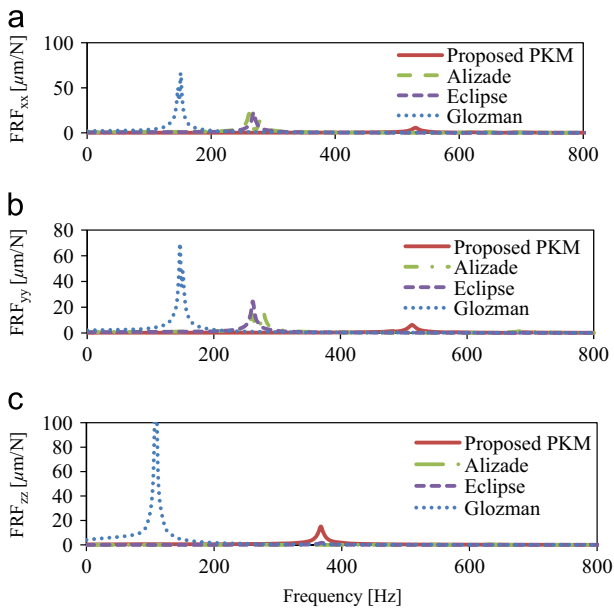


Fig. 10. FRF for all PKMs along the (a) xx, (b) yy, and, (c) zz directions.

Table 5
Minimum dynamic stiffness of all PKMs at home configuration.

Minimum dynamic stiffness	Proposed PKM	Eclipse PKM	Alizade PKM	Glozman PKM
K_{xx} [N/ μm]	0.178	0.044	0.047	0.015
K_{yy} [N/ μm]	0.161	0.041	0.071	0.021
K_{zz} [N/ μm]	0.066	0.567	2.08	0.005

4.2. Dynamic stiffness

The dynamic analysis of the proposed PKM presented in Section 3.3.2 is repeated here for all four PKMs with the dimensions specified in Table 3.

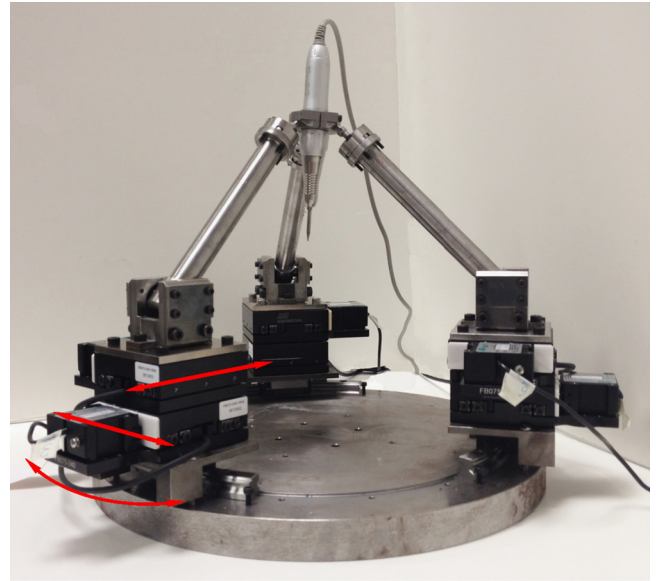


Fig. 11. 9-dof redundant reconfigurable 3xPPPRS RmMT.

Fig. 10(a) shows the magnitudes of the FRF of the PKMs along the x-axis, for a force that is applied in the same direction. Figs. 10 (b) and 10(c) show the FRFs of the PKMs in the y and z axes, for forces applied in the y and z axes, respectively. The same trends observed for the static stiffness, as given in Section 4.1, are noted here for the dynamic stiffness. The proposed PKM has the highest dynamic stiffness along the x and y axes, and the Eclipse and Alizade mechanisms have higher dynamic stiffness along the z-axis. Similar to the explanation given in Section 4.1, the dynamic stiffness of each PKM is decreased along the axis, on which the first links act as cantilever beams. For the Alizade mechanism, the chains are constructed from one prismatic kinematic coupling that connects the base and the platform. Hence, it does not include a link that acts as a cantilever beam, and it is stiffer along the z-axis.

The minimum dynamic stiffness values of the four PKMs are summarized in Table 5. Similar to the static stiffness, Table 5 shows that the proposed PKM architecture exhibits enhanced dynamic stiffness characteristics along the x- and y-axes. It should be noted, however, that although some differences in correlation between the static and dynamic stiffness exist, these can be attributed to the difference in the models used. For example, contrary to the dynamic stiffness, joint compliance has been incorporated in the static stiffness simulations. Also, for the static stiffness, the PKM configurations were optimized so as to achieve the highest stiffness along the x-axis whereas no optimization has been performed for the dynamic stiffness analysis.

5. Meso-milling machine prototype

A Reconfigurable meso-Milling Machine Tool (RmMT) prototype, shown in Fig. 11, was designed and built in our laboratory. A redundant reconfigurability approach was chosen for the developed RmMT [35]. Namely, all the required dof are incorporated into the machine, and reconfigurability is utilized through the locking/unlocking of the redundant dof.

The 9-dof RmMT is based on the proposed PKM, and its topology is denoted as $3 \times$ PPPRS. Namely, it consists of three identical chains, where each chain is attached to a stage that moves along a curvilinear guide. The curvilinear guide and stage unit chosen for the RmMT is the HCR 15A+60/150R made by THK Ltd. This stage can be moved to a desired location and then locked. Two FB075 linear stages, which are actuated by HR8 ultrasonic motors, manufactured by Nanomotion, are placed on top of the curvilinear stage. The structural components such as the base, links, and platform of the prototype are made from AISI 1018 steel.

The first linear stage moves tangentially with respect to the curvilinear guide, and the second linear stage, which is mounted on top of the first one, moves in radial direction. A revolute joint connects the linear stage with a fixed length link. The link is, then, connected on its other side through a Seiko Hephaist SRJ008C spherical joint, to the moving platform.

It should be noted that current commercially available spherical joints (e.g., Seiko Hephaist spherical joint) cannot achieve $\pm 70^\circ$ range of travel noted in Table 2. However, some examples for joints with large range of motions have been proposed in the academic literature [6], which can be used in meso-Milling applications. Thus, the $\pm 70^\circ$ used throughout the paper should be considered only for comparison between the mechanisms.

The built prototype was used as a test bed for integrating sub-components such as spindle, sensors and actuators. For example, a simple commercial spindle was incorporated into the center of the mobile tool platform, allowing for further study of the interaction between the spindle and the RmMT. In terms of human interface, the architecture of the RmMT allows for quick and easy access to the tool and workpiece. In addition, the mechanism is constructed such that the tool is supported from below, which allows for less interference between the spindle and the mechanism.

To further study the structural dynamic behavior of the prototype, Experimental Modal Analysis (EMA) was performed to obtain the FRFs of the reconfigurable $3 \times$ PPPRS RmMT prototype. An FEA simulation based on the detailed CAD model of the built prototype was performed. Fig. 12 compares the FRFs obtained from the experiments and those obtained from the FEA model of the

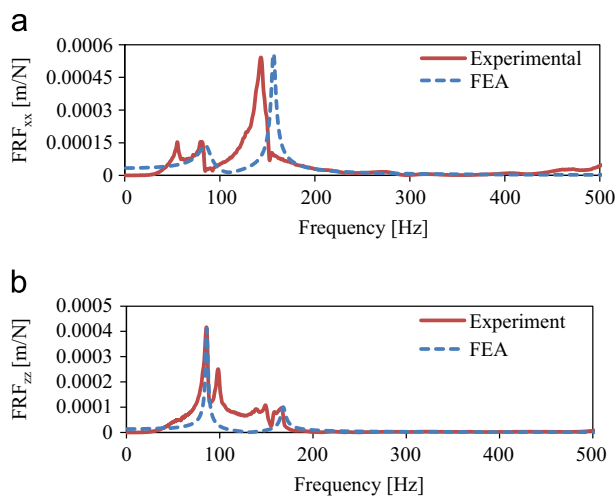


Fig. 12. Experimental and FEA data of the prototype along (a) x-axis, and (b) z-axis.

prototype for home configuration along x and z-axes. It is noted that the resonance frequencies and the FRF amplitudes of the experimental data are close to those obtained from the FEA model.

6. Conclusions

In this paper, a new 6-dof PKM architecture based on a $3 \times$ PPPRS topology was presented and its kinematics and dynamics were formulated. The platform tilt angle and stiffness of the proposed PKM were analyzed as a function of link length, and it was shown that the platform can tilt more than 90° . The static and dynamic stiffness of the proposed PKM was compared with three known PKMs, which can also attain more than 90° tilt angle. A statistical method was used to calculate the static stiffness distribution over the workspace, obtained from an analytical model. The dynamic stiffness of the PKMs was obtained via FEA. The results of both comparisons clearly indicate that the proposed PKM has superior static and dynamic stiffness.

Acknowledgment

The authors acknowledge the financial support of the NSERC Strategic Network – CANRIMT, and Promotion Ltd., Toronto, Canada for funding this research.

References

- [1] Weck M, Staimer D. Parallel kinematic machine tools – current state and future potentials. *CIRP Ann – Manuf Technol* 2002;51:671–83.
- [2] Altuzarra O, Martín YS, Amezcua E, Hernández A. Motion pattern analysis of parallel kinematic machines: a case study. *Robot Comput-Integr Manuf* 2009;25:432–40.
- [3] Y. Wang, W.S. Newman, Workspace analysis of the ParaDex robot – a novel, closed-chain, kinematically-redundant manipulator. In: Proceedings of the IEEE International Conference on Robotics & Automation, San Francisco, CA, USA; 2000. p. 2392–7.
- [4] J. Kotlarski, H. Abdellatif, B. Heimann, Improving the pose accuracy of a planar 3RRR parallel manipulator using kinematic redundancy and optimized switching patterns. In: Proceedings of the IEEE international conference on robotics and automation; 2008. p. 3863–8.
- [5] Robin V, Sabourin L, Gogu G. Optimization of a robotized cell with redundant architecture. *Robot Comput-Integr Manuf* 2011;27:13–21.
- [6] Valasek M, Zicha J, Karasek M, Hudec R. Hexasphere – redundantly actuated parallel spherical mechanism as a new concept of agile telescope. *Adv Astron* 2010;2010:1–6.
- [7] Gluzman D, Shoham M. Novel 6-dof parallel manipulator with large workspace. *Robotica* 2009;27:891–5.
- [8] Gogu G. Structural synthesis of parallelrobots part 1: methodology. Springer, P. O. Box 17, 3300 AA Dordrecht, The Netherlands; 2008.
- [9] Alizade RI, Tagiyev NR, Duffy J. A forward and reverse displacement analysis of a 6-dof in-parallel manipulator. *Mech Mach Theory* 1994;29:115–24.
- [10] Jongwon K, Chongwoo P, Sun Joong R, Jinwook K, Jae Chul H, Changbeom P, et al. Design and analysis of a redundantly actuated parallel mechanism for rapid machining, robotics and automation. *IEEE Trans* 2001;17:423–34.
- [11] Behi F. Kinematic analysis for a six-degree-of-freedom 3-PRPS parallel mechanism. *IEEE J Robot Autom* 1988;4:561–5.
- [12] Tahmasebi F, Tsai LW. On the stiffness of a novel six-dof parallel minimanipulator. In: *ISR*; 1995.
- [13] Ben-Horin R, Shoham M, Djerassi S. Kinematics, dynamics and construction of a planarily actuated parallel robot. *Robot Comput-Integr Manuf* 1998;14:163–72.
- [14] Azulay H, Hawryluck C, Mills JK, Benhabib B. Configuration design of a meso-milling machine, in: *Proceeding of the 23rd CADCAM Vancouver*; 2011.
- [15] Zhang D, Gosselin CM. Kinetostatic modeling of N-dof parallel mechanisms with a passive constraining leg and prismatic actuators. *ASME J Mech Des* 2001;123:375–81.
- [16] Gan D, Dai JS, Caldwell DG. Constraint-based limb synthesis and mobility-change-aimed mechanism construction. *ASME J Mech Des* 2011;133:051001–9.
- [17] Kong X, Gosselin CM. Type synthesis of 3-dof translational parallel manipulators based on screw theory. *ASME J Mech Des* 2004;126:83–92.
- [18] Merlet JP. *Parallel Robots*, 2nd ed., Springer, INRIA, Sophia-Antipolis, France; 2006.

- [19] Xiang Z, Hongya F, Zhenyu H, Yazhou S. 5-Axis micro-milling machine tool for machining complex 3D meso-scale parts. In: Proceedings of the international conference on mechatronics and automation; 2009. p. 4283–8.
- [20] Mahmoodi M, Le Y, Mills JK, Benhabib B. An active dynamic model for a parallel-mechanism-based meso-milling machine tool. In: Proceedings of the 23rd Canadian congress of applied mechanics (CANCAM), Vancouver, Canada; 2011.
- [21] Abdellatif H, Heimann B. Computational efficient inverse dynamics of 6-dof fully parallel manipulators by using the Lagrangian formalism. *Mech Mach Theory* 2009;44:192–207.
- [22] Khalil W, Ibrahim O. General solution for the dynamic modeling of parallel robots. In: Proceedings of the IEEE international conference on robotics and automation, New Orleans, LA, USA; 2004. p. 3665–70.
- [23] Sciavicco L, Siciliano B. Modeling and control of robot manipulators. 2nd ed.. New York: McGraw-Hill Companies; 2000.
- [24] Merlet JP. Jacobian, manipulability, condition number, and accuracy of parallel robots. *ASME J Mech Des* 2006;128:199–206.
- [25] Klimchik A, Pashkevich A, Caro S, Chablat D. Stiffness matrix of manipulators with passive joints: computational aspects. *Anglais* 2012;28:1–4.
- [26] Chanal H, Duc E, Ray P. A study of the impact of machine tool structure on machining processes. *Int J Mach Tools Manuf* 2006;46:98–106.
- [27] Majou Fe, Gosselin Ce, Wenger P, Chablat D. Parametric stiffness analysis of the orthoglide. *Mech Mach Theory* 2007;42:296–311.
- [28] Xu Q, Li Y. An investigation on mobility and stiffness of a 3-dof translational parallel manipulator via screw theory. *Robot Comput-Integr Manuf* 2008;24:402–14.
- [29] Aginaga J, Zabalza I, Altuzarra O, Nájera J. Improving static stiffness of the parallel manipulator using inverse singularities. *Robot Comput-Integr Manuf* 2012;28:458–71.
- [30] Deblaise D, Hernot X, Maurine P. A systematic analytical method for PKM stiffness matrix calculation. In: Proceedings of the 2006 IEEE international conference on robotics and automation, Orlando, Florida, USA; 2006. p. 4213–9.
- [31] Gosselin C. Stiffness mapping for parallel manipulators. *Anglais* 1990;6:377–82.
- [32] Wu J, Wang J, Wang L, You Z. Performance comparison of three planar 3-dof parallel manipulators with 4-RRR, 3-RRR and 2-RRR structures. *Mechatronics* 2010;20:510–7.
- [33] He J, Fu ZF. Modal analysis. Woburn, MA: Elsevier Science; 2001.
- [34] Cheng K. Machining dynamics: fundamentals, applications and practices. London: Springer; 2009.
- [35] Katz R. Design principles of reconfigurable machines. *Int J Adv Manuf Technol* 2007;34:430–9.